Simultaneous multi-parametric mapping of total sodium concentration, T1, T2 and ADC at 7 T using a multi-contrast unbalanced SSFP

Lisa Leroi, Arthur Coste, Ludovic de Rochefort, Mathieu D. Santin, Romain Valabregue, Franck Mauconduit, Eric Giacomini, Michel Luong, Edouard Chazel, Julien Valette, et al.

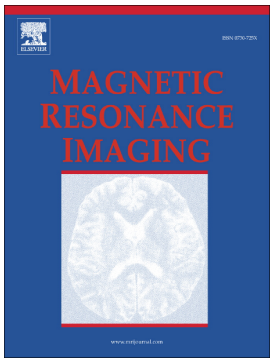

Simultaneous multi-parametric mapping of total sodium concentration, T1, T2 and ADC at 7 T using a multi-contrast unbalanced SSFP

Lisa Leroi, Arthur Coste, Ludovic de Rochefort, Mathieu D. Santin, Romain Valabregue, Franck Mauconduit, Eric Giacomini, Michel Luong, Edouard Chazel, Julien Valette, Denis Le Bihan, Cyril Poupon, Fawzi Boumezbeur, Cécile Rabrait-Lerman, Alexandre Vignaud

PII:	S0730-725X(18)30071-7
DOI:	doi:10.1016/j.mri.2018.07.012
Reference:	MRI 9007
To appear in:	*Magnetic Resonance Imaging*
Received date:	20 April 2018
Revised date:	23 July 2018
Accepted date:	23 July 2018

Please cite this article as: Lisa Leroi, Arthur Coste, Ludovic de Rochefort, Mathieu D. Santin, Romain Valabregue, Franck Mauconduit, Eric Giacomini, Michel Luong, Edouard Chazel, Julien Valette, Denis Le Bihan, Cyril Poupon, Fawzi Boumezbeur, Cécile Rabrait-Lerman, Alexandre Vignaud , Simultaneous multi-parametric mapping of total sodium concentration, T1, T2 and ADC at 7 T using a multi-contrast unbalanced SSFP. Mri (2018), doi:10.1016/j.mri.2018.07.012

Simultaneous multi-parametric mapping of Total sodium concentration, T_1, T_2 and ADC at 7 Tesla using a Multi-contrast unbalanced SSFP

Lisa Leroi[1†] & Arthur Coste[1†], Ludovic de Rochefort[2], Mathieu D. Santin[3-4], Romain Valabregue[3-4], Franck Mauconduit[5], Eric Giacomini[1], Michel Luong[1], Edouard Chazel[1], Julien Valette[6], Denis Le Bihan[1], Cyril Poupon[1], Fawzi Boumezbeur[1], Cécile Rabrait-Lerman[1], and Alexandre Vignaud[1]

[1] NeuroSpin, CEA, DRF/JOLIOT, Université Paris-Saclay, Gif-sur-Yvette, France

[2] CRMBM, UMR 7339, Aix-Marseille University, Marseille, France

[3] CENIR, Centre de NeuroImagerie de Recherche, Paris, France

[4] ICM, Inserm U 1127, CNRS UMR 7225, Sorbonne Universités, UPMC Université Paris 06 UMR S1127, Institut du Cerveau et de la Moelle épinière, Paris, France

[5]Siemens Healthineers, Saint-Denis, France

[6]Commissariat à l'Energie Atomique et aux Energies Alternatives (CEA), Direction de la Recherche Fondamentale (DRF), Institut de Biologie François Jacob, MIRCen, Fontenay-aux-Roses, France

Corresponding author: Alexandre Vignaud,

Address: CEA Saclay, Neurospin, Bat 145, 91191 Gif-sur-Yvette, France.

Email : alexandre.vignaud@cea.fr

Declarations of interest: none

Part of this work was (submitted/presented) at the ISMRM 2017 meeting.

Word count of the body of the text : 3461 words

[†] These authors contributed equally to this work

Simultaneous multi-parametric mapping of Total sodium concentration, T_1, T_2 and ADC at 7 Tesla using a Multi-contrast unbalanced SSFP

Abstract: (200 words)

Purpose: Quantifying multiple NMR properties of sodium could be of benefit to assess changes in cellular viability in biological tissues. A proof of concept of Quantitative Imaging using Configuration States (QuICS) based on a SSFP sequence with multiple contrasts was implemented to extract simultaneously 3D maps of applied flip angle (FA), total sodium concentration, T_1, T_2, and Apparent Diffusion Coefficient (ADC).

Methods: A 3D Cartesian Gradient Recalled Echo (GRE) sequence was used to acquire 11 non-balanced SSFP contrasts at a 6x6x6mm^3 isotropic resolution with carefully-chosen gradient spoiling area, RF amplitude and phase cycling, with TR/TE=20/3.2ms and 25 averages, leading to a total acquisition time of 1h18min. A least-squares fit between the measured and the analytical complex signals was performed to extract quantitative maps from a mono-exponential model. Multiple sodium phantoms with different compositions were studied to validate the ability of the method to measure sodium NMR properties in various conditions.

Results: Flip angle maps were retrieved. Relaxation times, ADC and sodium concentrations were estimated with controlled precision below 15%, and were in accordance with measurements from established methods and literature.

Conclusion: The results illustrate the ability to retrieve sodium NMR properties maps, which is a first step toward the estimation of FA, T_1, T_2, concentration and ADC of ^{23}Na for clinical research. With further optimization of the acquired QuICS contrasts, scan time could be reduced to be suitable with in vivo applications.

Between 3 to 6 key words: Non proton MRI; Sodium; T_1 mapping; T_2 mapping, Diffusion

1. INTRODUCTION

Sodium (^{23}Na) yields the second strongest NMR signal among biologically relevant NMR-active nuclei. ^{23}Na MRI offers insights into pathologies through novel metabolic information that classic proton MR imaging cannot access, potentially improving patient care in this way. Multiple publications deal with the investigation of sodium compartmentalization with the aim to separate intracellular ^{23}Na from the total sodium content as a marker of cell viability in vivo. However, the complexity to untangle such information makes these results debatable (1). Indeed, most of the studies are currently focusing on Total Sodium Concentration (TSC) which, non-exhaustively, has been shown to be beneficial to study tissue viability after stroke, to detect malignant tumors and to assess drug resistance before chemotherapy in rats glioma (2), Huntington's disease and multiple sclerosis in the brain, as well as acute myocardial infraction in the heart (3). In some studies, proton Diffusion-Weighted Imaging or contrast-enhanced MRI is also proposed and recommended to increase the sensitivity and specificity of the diagnosis (4). Thus, the opportunity to quantitatively retrieve ^{23}Na TSC in addition to several other NMR properties such as T_1, T_2 or Apparent Diffusion Coefficient (ADC) specific to ^{23}Na in a single experiment is of interest to improve the detection, the investigation of the physiopathology of various diseases and the evaluation of potential treatments, for an enhanced follow-up.

To date, the precise determination of the above-cited quantitative parameters requires the sequential implementation of several methods, as was demonstrated in the past (5–7). None of them addressed ^{23}Na DWI so far, as several challenges need to be tackled. First, 23Na very short relaxation times together with poor signal to noise ratio leads to a difficult detection. In addition, its 4-fold lower gyromagnetic ratio leads to approximately a 15-fold reduction in the effective b-values. Sodium diffusion has only been assessed in rat brain (8) and rat skeletal muscle using shift-reagent aided MR Spectroscopy (9). Therefore, the simultaneous, fast and robust mapping of ^{23}Na NMR properties constitutes a challenging, relevant and exciting prospect for biomedical research. For the mapping of ^{1}H, several methods have been developed recently to provide combined measurements of T_1 and T_2 (10–14) or T_2^*(15) and ADC (16,17) within a single acquisition. Some approaches use saturation pulses that are increasing the specific absorption rate and some require long and complex post-processing (18). Recently, a method to perform combined multi-parametric mapping of magnetization (M_0), flip angle (FA), global T_1, T_2 and mono-dimensional ADC altogether has been proposed (19,20). This technique, called Quantitative Imaging using Configuration States (QuICS), uses different contrasts generated from a Steady-State Free Precession (SSFP) sequence, by varying acquisition parameters such as phase cycling, spoiling gradient and FA. The multiple steady-states acquired then depend on the underlying physical parameters such as M_0, T_1, T_2, ADC and the actual FA. The simplified description using the configuration

states enables to precisely describe the signal under the Bloch-Torrey equation, and quantify the physical parameters through straightforward fitting (21,22). Although ^{23}Na is usually modeled using a density operator evolution under the Liouville equation, the magnetization behavior will be approximated to follow a single-T_2 simplified model weighted by its various contributions.

The aim of this work was to demonstrate the experimental feasibility of this approach on ^{23}Na to assess simultaneously in a single sequence total ^{23}Na NMR properties in phantoms experiments. It is performed at 7T to take advantage of the larger SNR (23). The robustness of the approach was evaluated in different physicochemical environments presenting variations of relaxation times, ADC and concentrations, corresponding to different in vivo tissues. To the knowledge of the authors, this phantom study is the first simultaneous multi-parametric quantitative extraction reported in the context of ^{23}Na MRI, and in particular the first 3D mapping of its ADC. Applicability to clinical acquisitions will be also discussed.

2. MATERIAL AND METHODS

2.1. Signal modeling and quantitative extraction principles

Balanced SSFP sequences are sensitive to B_0 inhomogeneity as the phase accumulated between two TRs is leading to the widely known banding-artifacts (24). Introducing a spoiling gradient G generally produces a much larger phase inhomogeneity such that the banding artifact becomes unapparent, as all phases between 0 and 2π are present within each voxel. Let us denote z the spoiling gradient axis. The gradient waveform $G(t)$ is chosen such that a constant area remains between two TRs. As shown in Eq. 1, this area is proportional to a spatial frequency shift Δk_z, and inversely proportional to a "spoiling distance", a, corresponding to a 2π dephasing between two TRs (Eq.1).

$$\Delta k_z = 1/a = \frac{\gamma}{2\pi}\int_0^{TR} G(t)\,dt \qquad \text{Eq.1}$$

In the sequence, we choose to parametrized this spoiling distance a as a ratio of the readout-pixel size Δz, using an integer *N* defined such that:

$$a = \frac{\Delta z}{N} \qquad \text{Eq.2}$$

To further indicate the amount of spoiling area applied respectively along the read-out, the phase encoding and slice selection directions, we introduce the numbers N_{RO}, N_{PE} and N_{SS}. Therefore, setting the parameters $N_{RO} \geq 1$, $N_{PE} = N_{SS} = 0$ in the sequence imposes the spoiling area along the read-out axis, and ensures that the sequence is spoiled with a dephasing superior to 2π over the pixel size.

In that framework, magnetization can be described in space or in terms of spatial frequencies. The latter description was proposed long ago and originally referred to as the configuration states description (25,26), similar to the extended phase graph description (27–30), and in which only discrete spatial frequencies are needed due to the constant dephasing between TRs. The longitudinal and transverse magnetization, M_z and M_{xy}, can respectively be decomposed into discrete Fourier series, as described in Eq.3 and Eq.4.

$$M_z = \sum_{k=-\infty}^{\infty} m_{z_k} Z^{-k} \qquad \text{Eq.3}$$

$$M_{xy} = \sum_{k=-\infty}^{\infty} m_{xy_k} Z^{-k} \qquad \text{Eq.4}$$

where k corresponds to the configuration state, also called "coherent" states in literature linked by "pathways" determined by the gradient dephasing. The complex exponential $Z = exp(-i2\pi.\Delta k_z.z)$ is introduced as a base function to describe the spatial modulations between two excitations. m_{z_k} and m_{xy_k} represent the coefficients of the discrete Fourier series.

After several excitations at constant RF amplitude, a steady-state is reached. As the spoiling distance *a* is chosen smaller than the voxel size, the measured signal corresponds to m_{xy_0}, the only non-vanishing term after averaging Eq.4 over the pixel size.

The steady state's contrast can then be manipulated using quadratic RF cycling. It was originally proposed by Zur and colleagues (31) to reduce stimulated echo formation and provide a steady-state closer to T_1-weighted fully spoiled sequences. It has been shown that very different steady-states can be obtained depending on the chosen spoiling increment, in particular with few degrees producing a strongly T_2-contrast (32–34). Therefore, the SSFP model is influenced by phase cycling. Its sensitivity is illustrated in Figure 1, which provides a representation of real and imaginary parts of m_{xy_0}, the steady-state transverse magnetization, depending on the spoiling phase increment value.

SSFP contrast can also be influenced by tissues properties such as T_1, T_2 and diffusion. In the configuration state description, T_1 and T_2 relaxations induce an attenuation of the magnetization components (29), while diffusion acts as Gaussian filtering (35,36). The full derivation of the steady-state signal, accounting for acquisition parameters as well as relaxation and free diffusion can be found in (19).

Figure 2 provides complex representations of signals obtained with different T_1, T_2, and ADC values for the same acquisition parameters, indicating that the SSFP model is sensitive to any variation of one of these physical parameters. Therefore, choosing appropriate N_{RO} and phase increments will allow a proper extraction of M_0, T_1, T_2 and ADC fitting the signal behavior.

To perform the quantitative extraction from the multiple SSFP contrasts, post-processing was performed using Matlab (The Mathworks, Natick, USA) and DICOM complex images. First, the acquired contrasts were grouped into a single measurement vector, S_{meas}. Global phase drifts were then removed, assuming a linear temporal evolution between the first and last volumes acquired in the same conditions. A gradient-echo phase map was estimated using the complex sum of volumes with 0° and 180° RF phase increments. It was then subtracted from all volumes providing the SSFP phase-induced maps corrected for the phase at echo time, and thus for B_0 inhomogeneities.

The quantification was then performed by a least-squares fit between S_{meas} and the model derived from Bloch-Torrey equation (19). A Gauss-Newton algorithm was implemented for that purpose, with a numerical evaluation of the Jacobian matrix, and an initialization step consisting in the comparison of S_{meas} with a dictionary of 50×50×30×20 values corresponding to R_1 = [0.01; 50]s^{-1}, R_2 = [0.01; 50]s^{-1} , ADC = [0.01; 3]x$10^{-3}$$mm^2.s^{-1}$ and FA = [0.045; 90]° covering expected range of values for ^{23}Na in the studied compositions. FA was considered as a variable to be determined here, as its degree of inhomogeneity can become large especially when using local transmit coils.

2.2. In-silico experimental setup formulation

In this study, only phase cycling was used to modulate the SSFP contrast. Thus, to determine the most adequate N_{RO} and FA to use to accurately assess the targeted sodium relaxations (T_1=60ms, T_2=50 ms) and ADC properties (ADC=1.3x10^{-3} mm²/s) under the scanning conditions described in the following section, simulations using brute-force Monte-Carlo SSFP were performed. The range of tested FA varied from 0 to 100° with a precision of 1°, using 10,000 samples per FA. To account for the coil receiving profile and associated FA and SNR variations, the voxel magnetization at thermal equilibrium, M_0, was proportionally adapted to the considered FA from empirical measurements. The range of tested N_{RO} varied from 1 to 47, corresponding to a diffusion sensitivity of b=TR*$(2\pi/a)^2$ ranging from 0.02 to 48.4 s.mm^{-2} between two RF pulses. The latter was the limit of our system given the chosen TR of 20ms and pixel size Δz = 6 mm.

2.3. MRI acquisitions

MRI acquisitions were performed on an investigational 7 Tesla MRI scanner (Siemens Healthineers, Erlangen, Germany) using a homemade hemi-cylindrical single channel Tx/Rx ^{23}Na coil (Figure 4a). FA was calibrated assuming that the reference voltage would allow to get a global mean FA equal to the targeted FA in the whole phantom. Acquisitions consisted in a repeated 3D non-selective Cartesian unbalanced SSFP with different contrasts. Scanning parameters were TR/TE=20ms/3.2ms, bandwidth=220Hz/px. The image resolution was 6mm^3 isotropic in a 192x192x160mm^3 field-of-view, and a pulse duration of 500µs. FA and N_{RO} were set respectively to 45° and 47, according to the results from the optimization process described above (see Figure 3). 11 contrasts were selected with RF spoiling increments = [0, 20, 100, 110, 130, 170, 190, 230, 250, 340, 360]° to sample the complex plane (Figure 1c). Using 25 averages, the acquisition time (TA) of a volume was 7 minutes, leading to a total TA of 1h18min.

MR spectroscopic measurements of ground-truth T_1, T_2 and ADC were performed on a 7 Tesla preclinical scanner (Pharmascan, Bruker, Ettlingen, Germany) using a small home-made dual-resonance ^{23}Na/^{1}H birdcage coil and gold-standard methods. Single Voxel Spectroscopy (SVS) data were acquired from a large 30 mm^3 voxel. For T_1 assessment, an Inversion Recovery (IR) LASER sequence (37,38) was used, varying the inversion time from 5 to 100ms by 10ms steps, with TR/TE=500/13ms, BW=4kHz and an inversion pulse of 2ms. Then, T_2 and ADC were measured using a STEAM sequence (39,40), acquiring respectively seventeen different TE from 2 to 120ms and five b-values from 0 to 1200 s/mm² with two diffusion gradient polarities to get rid of cross-terms with selection gradients. Acquisition parameters were set to TR/TM = 500/10ms, TE=10ms, BW=4kHz

and excitation pulse of 500µs. The consecutive SVS acquisitions for these three parameters took about 1h35min.

To test our method's ability to probe sodium NMR properties, experiments were conducted on a series on phantoms using the setup shown Figure 4a. First, three phantoms (150mL glass containers, diameter=3cm, Figure 4) containing the same CSF physiological NaCl concentration of 150mM were investigated, with 0, 2 and 5% agar gel to reduce the relaxation times of ^{23}Na, to mimic brain or cartilage properties. Second, to test the quantification of sodium concentrations, phantoms of 30, 50 and 100 mM NaCl were imaged with a reference tube of 150mM in the same configuration. Finally, to increase the viscosity of our saline solutions (41,42) and probe varying apparent ADCs of ^{23}Na, 5 to 15% w/w sucrose (Sigma-Aldrich, Saint Louis, USA) was added in the 150mL tubes.

MRS measurements were performed using tubes filled with similar compositions, using a concentration of 150mM NaCl. One reference tube was assessed, in addition with one tube containing 5% of agar gel and one containing 15% of sucrose.

2.4. Data analysis

Total sodium concentration maps were retrieved from the ratio between M_0 and B_1^-, where the sensitivity profile B_1^- was estimated from the FA distributions, by applying the reciprocity principle (43). The concentrations were estimated for each adjacent tube using the tube of 150mM as an external reference for concentration.

Due to the hemi-volumic coverage of our coil (Figure 4a), a substantial sensitivity bias was observed across our images. In order to limit the impact of this inhomogeneous SNR on the estimation of the NMR properties of ^{23}Na, a region-of-interest (ROI) was defined in each phantom to keep the upper part, where the FA was systematically higher than 40° (Figure 4b-f), as observed in the experimental setup formulation results (Figure 3). Estimations were performed by assessing the mean over the pixels respecting this criteria over the whole phantom, leading to robust estimations.

3. RESULTS

Results of the protocol optimization process are presented in Figure 3. It shows that FA and N_{RO} need to be respectively set to 45° and to 47, to get reliable estimations. As shown in Figure 4, regions of interests were also defined in each phantom to assess results where the FA was systematically higher than 40°.

As illustrated in Figure 5a, ^{23}Na concentrations were accurately estimated, relative quantification errors being below 15%. Likewise, the ADCs were estimated for the sucrose-enriched (5-15%w/w) saline phantoms (Figure 5b). SVS measurements lead to very similar results for both the reference and the 15% sucrose tubes.

To study the robustness of the method, different measurements were conducted varying the relaxation properties of the phantom using agar from 0 to 5%, to mimic different human tissue properties. Results displayed in Figure 5c show the consistency of the mean T_1 and total T_2 over the defined ROIs compared to SVS measurements. Similar values were also reported at 7T (44).

4. DISCUSSION

In this work, 3D simultaneous multi-parametric extraction of total sodium concentration and total T_2, T_1, ADC and flip angle at 7T was performed at 6mm^3 isotropic resolution in 1h18. To some extent, these maps are insensitive for B_0 heterogeneity, as these variations are accounted for in the model. Sodium concentrations corresponded to the preparations; relaxation rates were in agreement with MRS gold-standard measurements; ADC measurements were consistent with data and a measurable reduction in ADC was obtained while adding sucrose. The ^{23}Na ADC maps were estimated along a single spoiling gradient direction, assuming the diffusion weighting of a single quantum coherence NMR signal, which is relevant for most sodium ions in an isotropic media (8).

An acquisition protocol that allows reliable assessment of 3D quantitative maps was determined on the basis of our Monte-Carlo simulations (Figure 3). Data obtained during phantoms experiments validates this proof-of-concept acquisition set-up and demonstrates the feasibility of simultaneous multi-parametric quantitative extraction (Figure 4). Indeed, estimated relaxation times at 21°C were consistent with the presented gold-standard measurements using respectively IR-LASER for T_1 and STEAM for T_2 assessments and with values from literature obtained using non-localized Inversion-Recovery and spin-echo sequences at 22°C at 7T (44).

Large physiological concentrations variations were also studied, with an extraction of TSC leading to precision better than 15%. Diffusion estimations for reference saline solution tube is consistent with the gold-standard measurements. Despite an extensive interest for ^{23}Na diffusion in food processing (45–47), sodium diffusion assessment could be found in the chemistry literature at $1.300\pm0.005 \times 10^{-3} mm^2.s^{-1}$ using a conductimetric cell at 25°C for a 50mM saline solution (48). This value is consistent with our estimations, as temperatures are in a similar range and concentration should have limited effect on diffusion. Here, modifying viscosity with sucrose reduced ADC, as verified in spectroscopy and observed in ^{1}H literature (49).

We succeeded in assessing a large range of total sodium concentrations, relaxations and ADCs. The environments investigated here are usually studied in literature to mimic various in vivo tissues, from cartilage to brain. The relatively high standard deviations obtained in Figure 5b-d could be due to a low SNR from B_1^+ heterogeneity induced by the hemi-volumic Tx/Rx primate coil. The latter could be tackled using a birdcage coil to access the targeted angle more homogeneously. Simulations with lower SNR were also performed and demonstrate that a higher flip angle should be targeted in low SNR regions (See Supplementary Material).

^{23}Na has a peculiar sensitivity to its molecular environment through quadrupolar interactions. Therefore, its relaxation times exhibit bi-exponential curves in complex media such as tissues or agar gels. For T_1 relaxation, where short and long components accounts for respectively 20 and 80% of the ^{23}Na signal (50,51), the bi-exponential recovery is rarely observed, leading to the estimation of a mono-exponential T_1 ranging from 10 to 60ms. For T_2 relaxation, the respective contributions of its long ($T_{2\ long}$≈15-60ms) and short ($T_{2\ short}$ <5ms) components are considered to be about 40 and 60% of the signal respectively (at zero TE). These bi-exponential or mono-exponential relaxation times varies *in vivo* depending on the investigated tissue (52,53), its intracellular and extracellular volume fractions, and the sodium levels in those two compartments (53,54). The intracellular volume fraction is approximately 80% of the tissues with a sodium concentration of 10-15mM, and the extracellular volume fraction is around 20%, with a sodium concentration of 125-150mM. Like most ^{23}Na MRI approach aiming at the extraction of quantitative parameters, QuICS estimates apparent TSC, T_1, total T_2 and ADC reflecting the weighted sum of all those short, long, intra and extracellular components depending on the chosen acquisition parameters. In our case, given the long TE of 3.2ms, the total T_2 mainly reflects the long component of the T_2. Nevertheless, if any of the intra/extra or long/short T_2 compartments encounters fluctuations related to the metabolic state of the tissue or varying molecular environment of the sodium ions, one may expect QuICS to exhibit sensitivity to such variations, as other single parameter ^{23}Na qMRI techniques have already shown.

While one could regret this rather poor specificity, QuICS should compensate this weakness by finding specificity in the correlation of the multiple complementary NMR parameters, helping in the interpretation of the physio-pathological events. It can be considered as an alternative paradigm of investigation for 23Na data, comparable to strategies successfully applied with other simultaneous multi-parametric method in ^{1}H MRI (11,55), where the same kind of objections could be done regarding compartmentalization of water in biological tissues.

The experiments reported in this note present a proof-of-concept of the potential of QuICS approach to assess simultaneously a broad spectrum of ^{23}Na properties. To date, a combination of separate state-of-the-art TSC, T_1 and T_2 measurements at the spatial resolution we used is more competitive than what we propose (5–7). Nevertheless, we add a very important parameter, namely the ADC, which has a strong clinical potential to characterize ^{23}Na micro-environment. Additionally, acquisition time TA could be largely reduced in the future, performing an in-depth optimization of the acquisition protocol over FA, TR, N_{RO}, T_1, T_2 and ADC ranges to study the sensitivity and robustness of the method. For example, ADC required high spoiling gradients (Figure 3c). Using different N_{RO}, or equivalently different diffusion weighting b-values from one contrast to another, is expected to enhance the precision in the determination of the ADC coefficient (21). In the present study, only single direction ADC measurements has been performed along the readout axis. This was enough in the context of homogeneous phantoms, to be extended to an average global ADC. In vivo, this will not be the case in the vast majority of the organs and several spoiling directions will be mandatory to properly extract this parameter. Limiting the TA will require to only focus on selecting the most valuable steps playing with FA, RF and gradient spoiling including for the latest several orthogonal directions. Such an optimization has been demonstrated to be achievable using optimal design approaches based on reducing the Cramér-Rao lower bound (56,57). To reduce TA even more, non-Cartesian sampling sequence could be used to improve SNR. Combining such sampling strategy with a nonlinear iterative reconstruction algorithm would also provide an increase of SNR and enable sub-sampling to reduce TA (58–60). These improvements would be at the cost of a broadening of the effective Point Spread Function (PSF) in the reconstructed image, which can be optimized depending on the targeted application. The use of a birdcage coil to access the targeted FA more homogeneously over the region of interest, combined with a received-phase array coil to retrieve more signal would also help increasing available signal and further reduce TA or increase resolution (61). In the latter case, the sensitivity profile of the coil will be corrected using a post-processing algorithm to still be able to extract TSC (62). SAR simulations were carried out considering a reference voltage consistent with in vivo acquisitions on a dual resonant 1Tx/1Rx birdcage coil. For in vivo applications, the pulse duration would need to be lengthened to 700µs instead of 500µs to respect SAR international standards.

5. CONCLUSION

In conclusion, this work is the first application of a simultaneous multi-parametric estimation method to ^{23}Na nucleus. The method showed its ability to retrieve varying ^{23}Na concentrations, total relaxation times evolution and ADC. Measured parameters were in range of previously reported values in the literature and effective gold-standard measurements. Current acquisitions will be improved to reduce TA and resolution, while increasing SNR with the goal of obtaining a clinically-relevant scan time. The simultaneous quantitative assessment of several NMR physical parameters could pave the way to a new diagnostic process, where correlations between different tissues properties might lead to improve the patient outcome (11,55).

FIGURES LEGENDS

Figure 1. Real (a) and imaginary (b) part of the theoretical transverse magnetization signal for a voxel resulting for sodium physical constants T_1/T_2=60/50ms, ADC=1.3x10^{-3}mm²/s, and acquisition parameters TR=10ms, FA=45°, resolution of 6mm^3 and a constant spoiling gradient corresponding to N_{RO}=47 (a= 0.128mm). The associated complex plane is also displayed (c), where each cross corresponds to a different RF spoiling increment, sampled for each degree of from 0 to 360°. The maximum real value with null imaginary part corresponds to RF spoiling increment of 0°/360°.

Figure 2. Complex representation of simulated signals sampled for each degree of RF spoiling increment from 0 to 360°, TR=10ms, FA=45°, resolution of 6mm^3 and N_{RO}=47 (a=0.18mm) varying T_1(a), T_2(b) and ADC(c), otherwise fixed to respectively 60ms, 50ms and 1.3x10^{-3}mm²/s. This figure highlights the contrast variations that can be obtained depending on the relaxation times and diffusion.

Figure 3. Brute-force Monte-Carlo simulations of ^{23}Na T_1(a), T_2(b), ADC(c), M_0(d) and FA(e) estimations as a function of spoiling gradient moment (N_{RO}) applied in the readout direction and FA, in order to account for its variations due to the coil profile. TR was set to 20ms, RF spoiling increments = [0, 20, 100, 110, 130, 170, 190, 230, 250, 340, 360]°, pixel size Δz=6mm and expected T_1=60ms, T_2=20ms and ADC=1.3x10^{-3}mm².s^{-1}. To account for the coil receiving profile and associated FA and SNR variations, M_0 varied with FA. On the one hand, this figure illustrates that choosing a FA higher than 40° (shaded area) and the highest spoiling gradient momentum avoids bias and leads to the most accurate estimations for T_1, T_2 and ADC. In another hand, results obtained with FA below 40° and lower N_{RO} cannot be considered because a large bias and uncertainty in the estimations are observed. M_0 and FA estimations are more robust to FA variations, as a FA of 20° seems sufficient to estimate these parameters.

Figure 4. Schematic of our hemi-volumic ^{23}Na RF coil with positioning of phantoms (a) and multi-parametric transverse maps obtained using the QuICS method: ^{23}Na concentration (b), FA in degrees (c), T_1 and T_2 in ms (d, e) and ADC in 10^{-3}mm².s^{-1} (f). The white ROI delimits the region where FA>40°, in agreement with results on experimental setup formulation, Figure 3. In this experiment, tube 1 (left) contained saline water with a physiological CSF concentration of 150mM with 2% agar and tube 2 (right) contained the same saline water without agar. Total sodium concentration map was retrieved from the ratio between M_0 and B_1^-, where the sensitivity profile B_1^- was estimated from the FA distributions, by applying the reciprocity principle (60). The concentration for tube 2 was estimated using tube 1 as a reference. Over the ROI, results exhibit homogeneous and significantly different relaxation times between the two phantoms.

Figure 5. a) Expected dilution and experimental estimations obtained with QuICS for realistic total ^{23}Na concentrations. Measured concentrations tend to align with the first bisector (dashed line). b) Estimated ADC values at 21°C for four phantoms of 150mM NaCl and various sucrose mass fractions, with associated standard deviations. Results show a decreasing evolution of diffusion depending on sucrose concentration, confirming observations from (41,42,49) and DW-STEAM measurements. c) Estimated T_1 and T_2 for three phantoms of

150mM NaCl and various agar concentrations. As expected, relaxation times are decreased when adding agar. SVS-measurements are consistent with the QuICS estimations.

ACKNOWLEDGMENTS

This work was partly funded by the French program “Investissement d’Avenir” run by the ‘Agence Nationale pour la Recherche’; the grant reference is 'Infrastructure d’avenir en Biologie Santé - ANR-11-INBS-0006’.

REFERENCES

1. Thulborn KR. Quantitative sodium MR imaging: A review of its evolving role in medicine. NeuroImage 2018;168:250–268. doi: 10.1016/j.neuroimage.2016.11.056.

2. Schepkin VD, Bejarano FC, Morgan T, Gower-Winter S, Ozambela M, Levenson CW. In vivo magnetic resonance imaging of sodium and diffusion in rat glioma at 21.1 T. Magn. Reson. Med. 2012;67:1159–1166. doi: 10.1002/mrm.23077.

3. Madelin G, Regatte RR. Biomedical applications of sodium MRI in vivo. J. Magn. Reson. Imaging 2013;38:511–529. doi: 10.1002/jmri.24168.

4. Jacobs MA, Ouwerkerk R, Kamel I, Bottomley PA, Kim HS. Proton, Diffusion-weighted Imaging, and Sodium (23Na) MRI of Uterine Leiomyomata after MR-guided High Intensity Focused Ultrasound: A Preliminary Study. J. Magn. Reson. Imaging JMRI 2009;29:649–656. doi: 10.1002/jmri.21677.

5. Staroswiecki E, Nnewihe A, Bangerter NK, Daniel BL, Hargreaves BA. In Vivo Sodium Imaging and Relaxometry of the Breast at 3T. In: Proc. Intl. Soc. Mag. Reson. Med. 17; 2009. p. 2129.

6. Morrell G, Kaggie J, Stein M, parker S, Bangerter NK. Rapid high-resolution sodium relaxometry in human breast. In: Proc. Intl. Soc. Mag. Reson. Med. 24; 2016. p. 404.

7. Zbyn S, Juras V, Bogner W, Szomolanyi P, Welsch GH, Bittsansky M, Mlynarik V, Moser E, Trattnig S. Sodium in vivo measurement of T1 and T2* relaxation times of articular cartilage at 7 Tesla. In: Proc. Intl. Soc. Mag. Reson. Med. 17; 2009. p. 3997.

8. Goodman JA, Kroenke CD, Bretthorst GL, Ackerman JJH, Neil JJ. Sodium ion apparent diffusion coefficient in living rat brain. Magn. Reson. Med. 2005;53:1040–1045. doi: 10.1002/mrm.20444.

9. Babsky AM, Topper S, Zhang H, Gao Y, James JR, Hekmatyar SK, Bansal N. Evaluation of extra- and intracellular apparent diffusion coefficient of sodium in rat skeletal muscle: Effects of prolonged ischemia. Magn. Reson. Med. 2008;59:485–491. doi: 10.1002/mrm.21568.

10. Schmitt P, Griswold MA, Jakob PM, Kotas M, Gulani V, Flentje M, Haase A. Inversion recovery TrueFISP: Quantification of T1, T2, and spin density. Magn. Reson. Med. 2004;51:661–667. doi: 10.1002/mrm.20058.

11. Warntjes J b. m., Leinhard OD, West J, Lundberg P. Rapid magnetic resonance quantification on the brain: Optimization for clinical usage. Magn. Reson. Med. 2008;60:320–329. doi: 10.1002/mrm.21635.

12. Ma D, Gulani V, Seiberlich N, Liu K, Sunshine JL, Duerk JL, Griswold MA. Magnetic resonance fingerprinting. Nature 2013;495:187–192. doi: 10.1038/nature11971.

13. Heule R, Ganter C, Bieri O. Triple echo steady-state (TESS) relaxometry. Magn. Reson. Med. 2014;71:230–237. doi: 10.1002/mrm.24659.

14. Stöcker T, Keil F, Vahedipour K, Brenner D, Pracht E, Shah NJ. MR parameter quantification with magnetization-prepared double echo steady-state (MP-DESS). Magn. Reson. Med. 2014;72:103–111. doi: 10.1002/mrm.24901.

15. Warntjes J b. m., Dahlqvist O, Lundberg P. Novel method for rapid, simultaneous T1, T*2, and proton density quantification. Magn. Reson. Med. 2007;57:528–537. doi: 10.1002/mrm.21165.

16. Staroswiecki E, Granlund KL, Alley MT, Gold GE, Hargreaves BA. Simultaneous estimation of T2 and apparent diffusion coefficient in human articular cartilage in vivo with a modified three-dimensional double echo steady state (DESS) sequence at 3 T. Magn. Reson. Med. 2012;67:1086–1096. doi: 10.1002/mrm.23090.

17. Gras V, Farrher E, Grinberg F, Shah NJ. Diffusion-weighted DESS protocol optimization for simultaneous mapping of the mean diffusivity, proton density and relaxation times at 3 Tesla. Magn. Reson. Med. 2017;78:130–141. doi: 10.1002/mrm.26353.

18. Cloos MA, Knoll F, Zhao T, Block KT, Bruno M, Wiggins GC, Sodickson DK. Multiparametric imaging with heterogeneous radiofrequency fields. Nat. Commun. 2016;7:12445. doi: 10.1038/ncomms12445.

19. de Rochefort L. Method and device for imaging by magnetic resonance. 2016:WO 2016/180947 A1.

20. de Rochefort L. Encoding with Radiofrequency Spoiling, Equilibrium States and Inverse Problem for Parametric Mapping. In: Proc. Intl. Soc. Mag. Reson. Med. 23. ; 2015. p. 445.

21. de Rochefort L, Guillot G, Dubuisson R-M, Valabrègue R. In Vivo Feasibility of Multi-Parametric Mapping Based on Fast Steady-State Sequences. In: Proc. Intl. Soc. Mag. Reson. Med. 24; 2016. p. 1823.

22. Leroi L, de Rochefort L, Santin MD, Mauconduit F, Valabrègue R, de Sousa PL, Le Bihan D, Poupon C, Vignaud A. Simultaneous multiparametric quantitative extraction at 7 Tesla using QuICS. In: European Society for Magnetic Resonance in Medicine; 2016. p. 272.

23. Pohmann, Speck, Scheffler. Signal-to-noise ratio and MR tissue parameters in human brain imaging at 3, 7, and 9.4 tesla using current receive coil arrays. Magn. Reson. Med. 2015;75:801–809. doi: 10.1002/mrm.25677.

24. Epstein FH, Mugler JP, Brookeman JR. Spoiling of transverse magnetization in gradient-echo (GRE) imaging during the approach to steady state. Magn. Reson. Med. 1996;35:237–245. doi: 10.1002/mrm.1910350216.

25. Pauly J, Roux PL, Nishimura D, Macovski A. Parameter relations for the Shinnar-Le Roux selective excitation pulse design algorithm. IEEE Trans. Med. Imaging 1991;10:53–65. doi: 10.1109/42.75611.

26. Roux PL, Hinks RS. Stabilization of echo amplitudes in FSE sequences. Magn. Reson. Med. 1993;30:183–190. doi: 10.1002/mrm.1910300206.

27. Hennig J. Echoes—how to generate, recognize, use or avoid them in MR-imaging sequences. Part I: Fundamental and not so fundamental properties of spin echoes. Concepts Magn. Reson. 1991;3:125–143. doi: 10.1002/cmr.1820030302.

28. Hennig J. Echoes—how to generate, recognize, use or avoid them in MR-imaging sequences. Part II: Echoes in imaging sequences. Concepts Magn. Reson. 1991;3:179–192. doi: 10.1002/cmr.1820030402.

29. Scheffler K. A pictorial description of steady-states in rapid magnetic resonance imaging. Concepts Magn. Reson. 1999;11:291–304. doi: 10.1002/(SICI)1099-0534(1999)11:5<291::AID-CMR2>3.0.CO;2-J.

30. Weigel M. Extended phase graphs: Dephasing, RF pulses, and echoes - pure and simple. J. Magn. Reson. Imaging 2015;41:266–295. doi: 10.1002/jmri.24619.

31. Zur Y, Wood ML, Neuringer LJ. Spoiling of transverse magnetization in steady-state sequences. Magn. Reson. Med. 1991;21:251–263. doi: 10.1002/mrm.1910210210.

32. Ganter C. Steady state of gradient echo sequences with radiofrequency phase cycling: Analytical solution, contrast enhancement with partial spoiling. Magn. Reson. Med. 2006;55:98–107. doi: 10.1002/mrm.20736.

33. Bieri O, Scheffler K, Welsch GH, Trattnig S, Mamisch TC, Ganter C. Quantitative mapping of T2 using partial spoiling. Magn. Reson. Med. 2011;66:410–418. doi: 10.1002/mrm.22807.

34. de Sousa PL, Vignaud A, Caldas de Almeida Araújo E, Carlier PG. Factors controlling T2 mapping from partially spoiled SSFP sequence: Optimization for skeletal muscle characterization. Magn. Reson. Med. 2012;67:1379–1390. doi: 10.1002/mrm.23131.

35. Kaiser R, Bartholdi E, Ernst RR. Diffusion and field-gradient effects in NMR Fourier spectroscopy. J. Chem. Phys. 1974;60:2966–2979. doi: 10.1063/1.1681477.

36. Freed DE, Scheven UM, Zielinski LJ, Sen PN, Hürlimann MD. Steady-state free precession experiments and exact treatment of diffusion in a uniform gradient. J. Chem. Phys. 2001;115:4249–4258. doi: 10.1063/1.1389859.

37. Garwood M, DelaBarre L. The return of the frequency sweep: designing adiabatic pulses for contemporary NMR. J. Magn. Reson. 2001;153:155–177. doi: 10.1006/jmre.2001.2340.

38. Slotboom J, Mehlkopf AF, Bovée WMMJ. A single-shot localization pulse sequence suited for coils with inhomogeneous RF fields using adiabatic slice-selective RF pulses. J. Magn. Reson. 1991;95:396–404. doi: 10.1016/0022-2364(91)90229-M.

39. van Zijl PC, Moonen CT, Alger JR, Cohen JS, Chesnick SA. High field localized proton spectroscopy in small volumes: greatly improved localization and shimming using shielded strong gradients. Magn. Reson. Med. 1989;10:256–265.

40. Moonen CTW, Sobering G, Van Zijl PCM, Gillen J, Von Kienlin M, Bizzi A. Proton spectroscopic imaging of human brain. J. Magn. Reson. 1992;98:556–575. doi: 10.1016/0022-2364(92)90007-T.

41. Hara M, Kuroda M, Ohmura Y, Matsuzaki H, Kobayashi T, Murakami J, Katashima K, Ashida M, Ohno S, Asaumi J-I. A new phantom and empirical formula for apparent diffusion coefficient measurement by a 3 Tesla magnetic resonance imaging scanner. Oncol. Lett. 2014;8:819–824.

42. Winfield JM, Collins DJ, Priest AN, Quest RA, Glover A, Hunter S, Morgan VA, Freeman S, Rockall A, deSouza NM. A framework for optimization of diffusion-weighted MRI protocols for large field-of-view abdominal-pelvic imaging in multicenter studies. Med. Phys. 2016;43:95–110. doi: 10.1118/1.4937789.

43. Hoult DI. The principle of reciprocity in signal strength calculations—A mathematical guide. Concepts Magn. Reson. 2000;12:173–187. doi: 10.1002/1099-0534(2000)12:4<173::AID-CMR1>3.0.CO;2-Q.

44. Nagel AM, Umathum R, Rösler MB, Ladd ME, Litvak I, Gor'kov PL, Brey WW, Schepkin VD. 39K and 23Na relaxation times and MRI of rat head at 21.1 T. NMR Biomed. 2016;29:759–766. doi: 10.1002/nbm.3528.

45. Hansen CL, van der Berg F, Ringgaard S, Stødkilde-Jørgensen H, Karlsson AH. Diffusion of NaCl in meat studied by 1H and 23Na magnetic resonance imaging. Meat Sci. 2008;80:851–856. doi: 10.1016/j.meatsci.2008.04.003.

46. Bertram HC, Holdsworth SJ, Whittaker AK, Andersen HJ. Salt diffusion and distribution in meat studied by 23Na nuclear magnetic resonance imaging and relaxometry. J. Agric. Food Chem. 2005;53:7814–7818. doi: 10.1021/jf051017+.

47. Guiheneuf TM, Gibbs SJ, Hall LD. Measurement of the inter-diffusion of sodium ions during pork brining by one-dimensional 23Na Magnetic Resonance Imaging (MRI). J. Food Eng. 1997;31:457–471. doi: 10.1016/S0260-8774(96)00085-4.

48. Ribeiro ACF, Lobo VMM, Sobral AJFN, Soares HTFC, Esteso ARJ, Esteso MA. Diffusion coefficients of sodium fluoride in aqueous solutions at 298.15 k and 310.15 k. Acta Chim. Slov. 2010;57:410–414.

49. Laubach HJ, Jakob PM, Loevblad KO, Baird AE, Bovo MP, Edelman RR, Warach S. A Phantom for diffusion-weighted imaging of acute stroke. J. Magn. Reson. Imaging 1998;8:1349–1354. doi: 10.1002/jmri.1880080627.

50. Jaccard G, Wimperis S, Bodenhausen G. Multiple-quantum NMR spectroscopy of S=3/2 spins in isotropic phase: A new probe for multiexponential relaxation. J. Chem. Phys. 1986;85:6282–6293. doi: 10.1063/1.451458.

51. Zhang Y, Poirer-Quinot M, Springer CS, Balschi JA. Discrimination of intra- and extracellular 23Na+ signals in yeast cell suspensions using longitudinal magnetic resonance relaxography. J. Magn. Reson. San Diego Calif 1997 2010;205:28–37. doi: 10.1016/j.jmr.2010.03.018.

52. Ridley B, Nagel AM, Bydder M, et al. Distribution of brain sodium long and short relaxation times and concentrations: a multi-echo ultra-high field 23 Na MRI study. Sci. Rep. 2018;8:4357. doi: 10.1038/s41598-018-22711-0.

53. Foy BD, Burstein D. Interstitial sodium nuclear magnetic resonance relaxation times in perfused hearts. Biophys. J. 1990;58:127–134. doi: 10.1016/S0006-3495(90)82358-4.

54. Hutchison Robert B., Shapiro Joseph I. Measurement of intracellular sodium with NMR methods. Concepts Magn. Reson. 1991;3:215–236. doi: 10.1002/cmr.1820030404.

55. Yu AC, Badve C, Ponsky LE, et al. Development of a Combined MR Fingerprinting and Diffusion Examination for Prostate Cancer. Radiology 2017;283:729–738. doi: 10.1148/radiol.2017161599.

56. Valabrègue R, de Rochefort L. Fisher Information Matrix for Optimizing the Acquisition Parameters in Multi-Parametric Mapping Based on Fast Steady-State Sequences. In: Proc. Intl. Soc. Mag. Reson. Med. 24; 2016. p. 1569.

57. Zhao B, Haldar JP, Setsompop K, Wald LL. Optimal experiment design for magnetic resonance fingerprinting. In: 38th Annual International Conference of the IEEE Engineering in Medicine and Biology Society (EMBC). ; 2016. pp. 453–456. doi: 10.1109/EMBC.2016.7590737.

58. Coste A, Chauffert N, Vignaud A, Ciuciu P, Boumezbeur F, Weiss P, Romanzetti S, Le Bihan D, Lerman C. Assessment of benefit to use a non-Cartesian trajectory and nonlinear reconstruction method compared to a Cartesian strategy for fast 31P MRI. In: Proc. Intl. Soc. Mag. Reson. Med. 24; 2016. p. 3940.

59. Madelin G, Chang G, Otazo R, Jerschow A, Regatte RR. Compressed sensing sodium MRI of cartilage at 7T: Preliminary study. J. Magn. Reson. 2012;214:360–365. doi: 10.1016/j.jmr.2011.12.005.

60. Gnahm C, Nagel AM. Anatomically weighted second-order total variation reconstruction of 23Na MRI using prior information from 1H MRI. NeuroImage 2015;105:452–461. doi: 10.1016/j.neuroimage.2014.11.006.

61. Shajan G, Mirkes C, Buckenmaier K, Hoffmann J, Pohmann R, Scheffler K. Three-layered radio frequency coil arrangement for sodium MRI of the human brain at 9.4 Tesla. Magn. Reson. Med. 2016;75:906–916. doi: 10.1002/mrm.25666.

62. Santin MD. Pending Patent, #1759804/1000427656.